PHOTOELECTROCHEMICAL CHARACTERIZATION OF ANATASE-RUTILE MIXED TiO_2 NANOSPONGES

Fernández-Domene, R.M.; Sánchez-Tovar, R.; Sánchez-González, S.; García-Antón, J. *

Ingeniería Electroquímica y Corrosión (IEC). Departamento de Ingeniería Química y Nuclear. ETSI Industriales. Universitat Politècnica de València. Camino de Vera s/n, 46022 Valencia, Spain.

Tel. 34-96-387 76 32, Fax. 34-96-387 76 39, e-mail: jgarciaa@iqn.upv.es

Abstract

This work studies the influence of using hydrodynamic conditions during anodization on the morphology and electrochemical properties of anatase/rutile mixed TiO_2 nanotubes (Reynolds number, Re = 0) and nanosponges (Re > 0). To this purpose different techniques were used, such as: microscopy techniques (Field-Emission Scanning Electron Microscope, FE-SEM, and Confocal Laser-Raman Spectroscopy), Electrochemical Impedance Spectroscopy (EIS), Mott Schottky (MS) analysis and photoelectrochemical water splitting tests. This investigation demonstrates that the morphology of TiO_2 nanostructures may be greatly affected due to the hydrodynamic conditions and it can be adjusted in order to increase the efficiency for energy and environmental applications.

Keywords: anatase/rutile mixed TiO_2, hydrodynamic conditions, water splitting, Electrochemical Impedance Spectroscopy, Mott-Schottky analysis.

1. Introduction

In recent years, growing consideration has been given to the design and fabrication of nanostructured metal oxides because of their unique and promising properties and applications [1-27]. In this way, nanostructures can be tailored to possess a characteristic nanosize, high surface area and porosity.

Titanium dioxide, TiO_2, has many interesting properties that have turned it into the most studied compound for photochemical and photoelectrochemical purposes. TiO_2 nanostructures have a wide application in dye-sensitized solar cells and photocatalysis [1-6, 8, 9, 11, 14-18]. Moreover, TiO_2 nanostructures can be used to solve environmental problems, such as treatment and purification of polluted aqueous systems [7, 8, 12, 28].

In order to prepare TiO_2 nanostructures, various approaches have been reported, such as sol-gel techniques, hydrothermal methods, atomic-layer deposition, anodization, etc. [3]. Anodization allows fabricating highly ordered arrays of TiO_2 nanostructures in a controlled and reproducible way. Moreover, TiO_2 nanostructures formed by anodization grow directly on titanium, which is very useful, since it results in functional TiO_2 photoelectrodes that do not need to be compacted or sintered onto a back contact.

Recently, a new type of anodic nanosponges has been synthesized by means of electrochemical anodization of titanium under hydrodynamic conditions [15, 18]. This synthesis route provides photoelectrodes with high specific surface area and a direct connected path for electrons, properties that make nanosponges be suitable for their use

in photoelectrochemical applications.

In the present work, the influence of Reynolds number (Re) on the morphology and electrochemical properties of anatase/rutile mixed TiO_2 nanotubes (Re = 0) and nanosponges (Re > 0) has been studied by using different microscopy techniques (Field-Emission Scanning Electron Microscope, FE-SEM, and Confocal Laser-Raman Spectroscopy), Electrochemical Impedance Spectroscopy (EIS), Mott Schottky (MS) analysis and photoelectrochemical water splitting tests. This investigation demonstrates that the morphology of TiO_2 nanostructures may be greatly affected due to the hydrodynamic conditions and it can be adjusted in order to increase the efficiency for energy and environmental applications.

2. Experimental procedure

Titanium samples were cylinders 8 mm in diameter and with 99.3% purity. Prior to the anodization process, the titanium rod surface was abraded with 500 to 4000 silicon carbide (SiC) papers, in order to obtain a mirror finish. After this, the sample was sonicated in ethanol for 2 min and dried in a N_2 stream. The polished Ti samples were anodized in a glycerol/water (60:40 vol.%) electrolyte containing 0.27 M NH_4F, at different Reynolds number (from Re = 0 to Re = 500) and at room temperature, by increasing the potential from zero to 30 V at a rate of 200 mV s^{-1}, applying subsequently the potential of 30 V for 3 hours. Anodization was performed in a conventional two-electrode cell with a rotating electrode configuration and a platinum mesh as counter electrode. The active anode area exposed to the electrolyte was 0.5 cm^2. During the process, anodization current density was monitored with a computer.

After anodization, the sample was washed with distilled water and ethanol and then dried in a N_2 stream. Finally, the as-anodized samples were annealed at 650º C for 1 hour in air atmosphere.

After each test, a Field-Emission Scanning Electron Microscope (FE-SEM) was used for morphological characterization of the obtained samples. The materials were also examined by Raman spectroscopy (Witec Raman Confocal microscope) after the heat treatment, in order to evaluate their crystalline structure. For these measurements the samples were illuminated with a 632 nm neon laser using 420 μW.

For the electrochemical and photoelectrochemical water splitting tests, a three-electrode configuration was used. The area of the TiO_2 nanostructures (working electrode) exposed to the test solution was 0.13 cm^2. A saturated Ag/AgCl (3 M KCl) electrode was the reference electrode, and a platinum tip was the counter electrode. The electrochemical measurements were conducted in a 0.1 Na_2SO_4 solution using an Autolab PGSTAT302N potentiostat under dark conditions (without irradiation). EIS experiments were conducted over a frequency range from 100 kHz to 10 mHz with a 10 mV (peak to peak) signal amplitude. MS plots were subsequently obtained by sweeping the potential from the open circuit potential in the negative direction at 10 mV s^{-1} with an amplitude signal of 10 mV at a frequency value of 10 kHz.

The photoelectrochemical experiments were carried out under simulated sunlight condition AM 1.5 (100 mW cm^2) in a 1M KOH solution. Photocurrent vs. potential characteristics were recorded by scanning the potential from −0.8 $V_{Ag/AgCl}$ to 0.5 $V_{Ag/AgCl}$ with a scan rate of 2 mV s^{-1}. Photocurrent transients as a function of the

applied potential were recorded by chopped light irradiation (60 s in the dark and 20 s in the light). Samples were left at 0.5 $V_{Ag/AgCl}$ in the light for one hour, in order to evaluate their resistance to undergo photocorrosion attacks.

3. Results and discussion

3.1. Current density transients during anodization

The formation and growth of the TiO_2 nanostructures was monitored by recording the current density-time behavior (**Figure 1**). Current density transients shown in **Figure 1** were obtained once the final potential of 30 V was reached, after applying a potential ramp of 200 mV s^{-1} from a potential of zero to 30 V. During the first seconds of anodization at 30 V (stage I in **Figure 1**), the current density decreased sharply, indicating the growth of an anodic TiO_2 layer on the electrode surface. After this initial stage, an increase in current density indicated the onset of TiO_2 dissolution due to the presence of fluoride ions in the electrolyte (stage II), according to the following reaction [3, 29]:

$$TiO_2 + 6F^- + 4H^+ \rightarrow [TiF_6]^{2-} + 2H_2O \quad \textbf{(1)}$$

In stage II, the TiO_2 dissolution by the F^- attack was highly localized, and irregular nanoscale pits nucleated throughout the electrode surface. After that, the current density reached a local maximum and started decreasing and increasing again, eventually taking constant values (stage III), indicating the establishment of a steady state between the

rate of TiO_2 formation and dissolution by the action of F^-. It was in this third stage that the formation of a regular nanotube or nanosponge layer took place.

It can be observed from **Figure 1** that current densities increased, in general, with increasing Re, in each of the three stages described above, indicating that hydrodynamic conditions enhanced the electrochemical processes taking place during anodization, especially the growth of a nanostructured layer at a steady state current density. The increase in current density in the last stage is more marked when changing from Re = 0 to Re = 100 than at different Re > 0. Hence, the formation of nanosponges ocurred at high reaction rates than nanotubes. As it will be commented in the next section, these high reaction rates are directly related to an increase in the active area of nanosponges with respect to nanotubes.

3.2. Morphological characterization by means of Field Emission Scanning Electron Microscopy (FE-SEM)

The anodized nanostructures were morphologically characterized using a FE-SEM and the obtained results are presented in **Figure 2**. Clearly, two different morphologies are determined by the use of hydrodynamic conditions during anodization. First, under static conditions, **Figure 2a** shows a nanotubular morphology typical of self ordered nanotubes (**Figure 2b**) grown in glycerol-water electrolytes [30, 31], with irregular open pores (140-230 nm), which does not present an initiation layer or nanograss. On the other hand, under stirring conditions (Re > 0) the nanotubular morphology is changed to anodic nanosponge, which is characterized by a connected and highly porous TiO_2 structure with pore openings of approximately 50 nm (**Figures 2c-g** and

Figure 2h, top and cross sectional views, respectively). According to **Figure 2**, the porosity of the nanosponges seems to increase with Re.

Additionally, the effect of hydrodynamic conditions is to increase the thickness of the nanostructures from approximately 1.7 μm for the nanotubes (Re = 0) to roughly 4.4 μm for the nanosponges synthesized at Re = 500 (**Figure 3**). However, the increase in the thickness of the layers is more pronounced from Re = 100 to Re = 200 (2 to 3.9 mm, respectively).

3.3. Characterization of the crystallinity of the nanostructures by means of Raman Confocal Laser Microscopy

Raman Confocal Laser microscopy was used in order to determine the crystalline phases of the nanostructures. The nanostructures before the heat treatment consisted of amorphous TiO_2, since no peaks were registered in the Raman measurements. **Figure 4** shows, as an example, the Raman spectra of the amorphous nanotubes anodized at Re = 0. On the other hand, annealing the samples at 650 ºC for 1 hour in air produces the crystallinity of TiO_2 in both anatase and rutile phases. In this way, **Figure 4** shows, for instance, the Raman spectra corresponding to the obtained nanotubes (anodized at Re = 0) and nanosponges (anodized at Re = 500), where the characteristic peaks of anatase and rutile phases are presented; i.e. the five allowed modes of anatase: 143 cm^{-1} (E_g), 197 cm^{-1} (E_g), 395 cm^{-1} (B_{1g}), 517 cm^{-1} (A_{2g}) and 638 cm^{-1} (E_g) (indicated as A in **Figure 4**) [32, 33] and the rutile peaks: 144 cm^{-1} (superimposed with the 143 cm^{-1} peak of anatase phase) (B_{1g}), 235 cm^{-1} (two-phonon scattering), 445 cm^{-1} (E_g) and 612 cm^{-1} (A_{1g}) (indicated as R in **Figure 4**) [33, 34].

3.4. Electrochemical characterization

3.4.1. EIS measurements

EIS measurements were carried out in a 0.1M Na_2SO_4 solution at open circuit potential under dark conditions and at 25º C, in order to characterize the electrochemical properties of the nanotubes and nanosponges formed at different Re. **Figure 5** shows the experimental Nyquist (**Figure 5a**), Bode-phase (**Figure 5b**) and Bode-module (**Figure 5c**) plots for the nanostructures, together with a diagram of the equivalent circuit used to fit the EIS data (**Figure 5d**).

Regarding the information provided in the Nyquist plots, all the TiO_2 nanostructures possess one or two distorted small semicircles at high and intermediate frequencies followed by an unfinished semicircle at low frequencies, with higher amplitude. The amplitude of the small semicircle obtained at high frequencies is lower for the nanotubes anodized at Re = 0, and in general, the amplitude of the semicircle decreases with Re (see inset of **Figure 5a**). Additionally, the Bode-phase plots reveal the presence of three time constants. For the nanosponges anodized at Re = 500, only two peaks can be clearly observed in the Bode-phase plots (one at high-intermediate frequencies and another at low frequencies). This is due to the fact that the peak at intermediate frequencies involves the two time constant presented for the rest of nanostructures at high-intermediate frequencies.

In order to explain the obtained EIS data, an equivalent electrical circuit with three RC time constants was proposed (**Figure 5d**). Constant phase elements (*CPEs*) have been used instead of pure capacitors to account for frequency dispersion and non-ideality.

The elements proposed for the equivalent circuit are: the electrolyte resistance (R_S), the first time constant (R_1CPE_1), which is related to the TiO_2 nanoporous/nanotubular structure [11, 35-38], the second time constant (R_2CPE_2), associated with the rutile layer accumulated at the bottom of the nanostructures array and the third time constant (R_3CPE_3), related to the compact TiO_2 layer formed beneath the nanostructures arrays [6, 39]. The presence of rutile after annealing the samples at 650 ºC during 1 h was confirmed using the Raman Confocal microscope. During the heat treatment, the walls of the TiO_2 nanostructures transform into anatase phase whereas a layer at the bottom transforms into rutile [1, 40, 41].

The values of the equivalent circuit parameters are shown in **Table 1**, where *CPEs* have been converted into pure capacitances, *C*, by using the following equation [42, 43]:

$$C = \frac{(Q \cdot R)^{1/\alpha}}{R} \quad \textbf{(2)}$$

where *Q* is the impedance of the *CPE* and *R* corresponds to R_2 and R_3 when determining capacitance values of the second and third time constants in **Figure 5d**. To determine C_1 from CPE_1, *R* has been calculated as follows:

$$\frac{1}{R} = \frac{1}{R_S} + \frac{1}{R_1} \quad \textbf{(3)}$$

According to **Table 1**, the values of R_s for all the nanostructures are almost constant (around 43 $\Omega \cdot cm^2$). The values corresponding to R_1, R_2 and R_3 are of the order of $k\Omega \cdot cm^2$. The higher values of R_3 are consistent with the resistance of a compact TiO_2

layer. The values of the resistance of the rutile layer (R_2) are much lower than the corresponding to a compact TiO_2 layer but higher than the resistance values of the anatase nanostructures arrays (R_1). This is in agreement with the lower conductivity of the rutile phase compared to the anatase one [3, 44, 45]. **Table 1** also shows that the values of R_1 and R_2 (resistance corresponding to the array-bottom of the nanostructures) decrease under hydrodynamic conditions, indicating that the nanosponges possess higher electrical conductivity and surface area than the nanotubes formed under stagnant conditions. No clear tendency of R_3 values is observed with Re, indicating that the electrical properties of the compact TiO_2 underlayer are not dependant on the hydrodynamic conditions.

The values of α for each of the phase constants are not affected by the flowing conditions and remain almost constant regardless of the Re. On the other hand, C_1 values are lower than those of C_2, and the C_3 values are considerably higher than the C_2 ones, regardless of the value of Re. Additionally, all the capacitance values are higher for the nanosponges in comparison to the nanotubes. This could be associated with a decrease in the thickness of the particular layer or by an increase in the porosity of this layer as a consequence of a transition to a more porous layer in the case of the nanosponges [6, 39]. In this particular case, since the thickness of the nanosponges is higher than the corresponding to the nanotubes (**Figure 3**), the increase in C_1 and C_2 with Re can be related to a higher porosity of the nanosponges.

3.4.2. MS analysis

To study the influence of hydrodynamic conditions during the formation of TiO_2 nanostructures on their electronic properties, the electrochemical capacitance of the TiO_2 photoanode/electrolyte interfase was measured as a function of the applied potential. Mott-Schottky analysis was performed to obtain the donor density, N_D, as well as the flat-band potential, U_{FB}, of the anatase/rutile mixed TiO_2 nanotubes and nanosponges formed at different Re. The total capacitance has been calculated from the imaginary component of the impedance (Z'') using the relationship $C = -1/\omega Z''$, where ω is the angular frequency. MS plots have been obtained at a frequency of 10 kHz since at this high value the capacitance dependence on frequency is eliminated [18, 46, 47].

Figure 6 shows the MS plots at a frequency of 10 kHz of the different TiO_2 nanostructures. The positive slopes of the MS plots are characteristic of n-type semiconductors, with the dominant defects being oxygen vacancies [11, 16, 48-51]. The MS equation for *n*-type semiconductors:

$$\frac{1}{C^2} = \frac{2}{\varepsilon_r \varepsilon_0 e N_D}\left(U - U_{FB} - \frac{kT}{e}\right) \quad \textbf{(4)}$$

where ε_r represents the relative dielectric constant of the TiO_2 nanostructures (a value of 100 has been assumed [14, 16, 18]), ε_0 is the vacuum permittivity ($8.85 \cdot 10^{-14}$ F cm^{-1}), e is the electron charge ($1.60 \cdot 10^{-19}$ C), N_D is the donor density, U_{FB} is the flat-band potential, k is the Boltzmann constant ($1.38 \cdot 10^{-23}$ J K^{-1}) and T is the absolute temperature.

The values of N_D and U_{FB} are presented in **Table 2** for the anatase/rutile mixed TiO_2 nanostructures synthesized at different Re. The results show that N_D values are of the order of 10^{17} cm^{-3}, which are two orders of magnitude lower than the values obtained for anatase TiO_2 nanotubes and nanosponges in a previous work [18], indicating that the anatase/rutile nanotubes and nanosponges have a lower degree of defectiveness than their anatase counterpart. It can also be observed that N_D decreases with increasing Re, that is, nanosponges formed under hydrodynamic conditions are less defective than nanotubes formed under static conditions. This decrease in the number of donor states did not negatively affect the conductivity of nanosponges, which has been observed to increase with Re (decrease in R_1, **Table 1**). Oxygen vacancies have been reported to act as recombination centers for electron and holes when they behave as deep donors, playing a critical role in the trapping process [17, 52, 53]. Hence, oxygen vacancies may favor the photoelectron activation or they may act as recombination centers, hindering the generation of photocurrent [17, 27].

The flat-band potential, U_{FB}, is the potential that needs to be applied over the semiconductor/electrolyte interface to make the energy bands remain flat. This potential indicates the position of the semiconductor Fermi level with respect to the used reference electrode. In *n*-type semiconductors the Fermi level is close to the conduction band, so the value of the U_{FB} is an indication of the position of the conduction band lower edge. This potential is also related to the potential difference in the space charge region ($\Delta\phi_{SC}$) that develops inside the semiconductor when in contact with an electrolyte:

$$\Delta\phi_{SC} = U_A - U_{FB} \quad \textbf{(5)}$$

where U_A is the external potential applied to the system. It is clear that for a given value of U_A, the more negative the value of U_{FB}, the higher (more positive) the value of $\Delta\phi_{SC}$. This potential drop is directly related to the electric field strength within the space charge layer, which is the driving force to attain a proper separation of the photogenerated electron-hole pairs. Hence, the more negative the value of U_{FB}, the better the charge separation inside the semiconductor and the lower the electron-hole recombination probability [17, 18, 46].

According to eq. (4), U_{FB} can be determined from the intercept of the straight line in the MS plots with the potential axis and its values for anatase/rutile mixed TiO_2 nanotubes and anosponges are shown in **Table 2**. It can be observed that U_{FB} becomes more negative with increasing Re. Therefore, according to the previous explanations, the recombination probability decreases for nanosponges with respect to nanotubes. This is consistent with the lower values of N_D obtained for nanosponges, since oxygen vacancies may behave as recombination sites and, thus, a slight decrease in N_D can be beneficial.

Furthermore, compared with the same TiO_2 nanostructures, but containing only anatase phase [18], the anatase/rutile mixed TiO_2 nanotubes and nanosponges possess more negative values of U_{FB}. These results also indicate that a mixture of anatase/rutile is better than only anatase in terms of reducing the recombination probability.

3.5. Photoelectrochemical performance

Figure 7 shows the measured current density of the nanotubes and nanosponges arrays with respect to the applied potential, under dark and illumination (photocurrent) conditions. It can be observed that upon illumination, all the samples gave a photocurrent response. An increase in photocurrent can be observed with increasing Re, indicating that the photoelectrochemical performance of nanosponges is better than that of nanotubes. This can be explained in terms of higher active areas in nanosponges. Besides, as commented above, the lower values of N_D and the more negative values of U_{FB} obtained for nanosponges also indicate that the recombination probability decreases with increasing Re.

Comparing these values with those obtained for anatase TiO_2 nanotubes and nanosponges [18] (notice that in this previous work, the highest used Re was 400, so values for Re = 500 have not been taken into account in these comparison), it can be observed that for the same Re, photocurrent densities are slightly higher in the present study (**Table 3**), indicating that the formation of a mixed anatase/rutile phase in the nanotubes and nanosponges somewhat enhanced the photoelectrochemical performance of the samples. This result is in accordance with the lower recombination probability of the anatase/rutile mixed nanostructures observed above.

The resistance of the formed TiO_2 nanostructures to photocorrosion was studied by recording the photocurrent at an applied constant potential of 0.5 $V_{Ag/AgCl}$ for 1 hour. **Figure 8** shows that photocurrents barely changed with irradiation time, indicating that

anatase/rutile mixed TiO_2 nanotubes and nanosponges were resistant to degradation and photocorrosion in the studied electrolyte (1M KOH).

4. Conclusions

Two different morphologies were determined by the use of hydrodynamic conditions during anodization in glycerol-water-ammonium fluoride electrolytes. FE-SEM revealed that under static conditions, self ordered nanotubes were grown whereas under flowing the nanotubular morphology is changed to nanosponge. The thickness and the porosity of the nanostructures increase with Re, which is in accordance with the higher current densities obtained during anodization with increasing Re.

Raman Confocal Laser microscopy shows that annealing the samples at 650 ºC for 1 hour in air produces the crystallization of TiO_2 in both anatase and rutile phases.

According to the values of the resistances obtained by EIS, the values of resistances corresponding to the array-bottom of the nanostructures decrease under hydrodynamic conditions, indicating that the nanosponges possess higher electrical conductivity and surface area than the nanotubes formed under stagnant conditions. Additionally, all the capacitance values increase with Re, this fact can be related, in this case, to a higher porosity of the nanosponges.

The density of donor species, N_D (mainly oxygen vacancies), was found to decrease with increasing Re, that is, nanosponges formed under hydrodynamic conditions were less defective than nanotubes formed under static conditions. Besides, N_D decreased

with respect to the values obtained for anatase TiO_2 nanostructures. On the other hand, U_{FB} became more negative with increasing Re, indicating that the recombination probability decreased for nanosponges with respect to nanotubes. Moreover, the anatase/rutile mixed TiO_2 nanostructures possessed more negative values of U_{FB} than anatase TiO_2 nanostructures, which also indicates that a mixture of anatase/rutile is better than only anatase in terms of reducing the recombination probability.

An increase in photocurrent was observed with increasing Re, indicating that the photoelectrochemical performance of nanosponges was better than that of nanotubes, because of the higher active areas of nanosponges and their lower recombination probability. On the other hand, photocurrent values for anatase/rutile mixed TiO_2 nanostructures were slightly higher than that for anatase TiO_2 nanostructures, meaning that the former system presents better photoelectrochemical performance than the latter one.

Acknowledgements: Authors would like to express their gratitude for their financial support to the Ministerio of Economía y Competitividad (Project CTQ2013-42494-R).

REFERENCES

[1] G. K. Mor, O. K. Varghese, M. Paulose, K. Shankar, C. A. Grimes. A review on highly ordered, vertically oriented TiO_2 nanotube arrays: Fabrication, material properties, and solar energy applications, Sol. Energy Mater. Sol. Cells 90 (2006) 2011.

[2] J. M. Macak, H. Tsuchiya, A. Ghicov, K. Yasuda, R. Hahn, S. Bauer, P. Schmuki. TiO_2 nanotubes: Self-organized electrochemical formation, properties and applications, Curr. Opin. Solid St. Mater. Sci. 11 (2007) 3.

[3] P. Roy, S. Berger, P. Schmuki. TiO_2 Nanotubes: Synthesis and Applications, Angew. Chem. Int. Ed. 50 (2011) 2904.

[4] H. E. Prakasam, K. Shankar, M. Paulose, O. K. Varghese, C. A. Grimes. A New Benchmark for TiO_2 Nanotube Array Growth by Anodization, J. Phys. Chem. C 111 (2007) 7235.

[5] A. G. Muñoz, Q. Chen, P. Schmuki. Interfacial properties of self-organized TiO2 nanotubes studied by impedance spectroscopy, J. Solid State Electrochem. 11 (2007) 1077.

[6] A. G. Muñoz. Semiconducting properties of self-organized TiO_2 nanotubes, Electrochim. Acta 52 (2007) 4167.

[7] G. Zhang, H. Huang, Y. Zhang, H. L. W. Chan, L. Zhou. Highly ordered nanoporous TiO_2 and its photocatalytic properties, Electrochem. Commun. 9 (2007) 2854.

[8] D. Wang, Y. Liu, B. Yu, F. Zhou, W. Liu. TiO_2 Nanotubes with Tunable Morphology, Diameter, and Length: Synthesis and Photo-Electrical/Catalytic Performance, Chem. Mater. 21 (2009) 1198.

[9] R. Abe. Recent progress on photocatalytic and photoelectrochemical water splitting under visible light irradiation, J. Photoch. Photobio. C 11 (2010) 179.

[10] P. Pu, H. Cachet, E. M. M. Sutter. Electrochemical impedance spectroscopy to study photo-induced effects on self-organized TiO_2 nanotube arrays, Electrochim. Acta 55 (2010) 5938.

[11] S. Palmas, A. M. Polcaro, J. R. Ruiz, A. Da Pozzo, M. Mascia, A. Vacca. TiO_2 photoanodes for electrically enhanced water splitting, Int. J. Hydrogen Energ. 35 (2010) 6561.

[12] X. He, Y. Cai, H. Zhang, C. Liang. Photocatalytic degradation of organic pollutants with Ag decorated free-standing TiO_2 nanotube arrays and interface electrochemical response, J. Mater. Chem. 21 (2011) 475.

[13] P. Acevedo-Peña, I. González. TiO_2 Nanotubes Formed in Aqueous Media: Relationship between Morphology, Electrochemical Properties and the

Photoelectrochemical Performance for Water Oxidation, J. Electrochem. Soc. 160 (2013) H452.

[14] L.-K. Tsui, T. Homma, G. Zangari. Photocurrent Conversion in Anodized TiO_2 Nanotube Arrays: Effect of the Water Content in Anodizing Solutions, J. Phys. Chem. C 117 (2013) 6979.

[15] R. Sánchez-Tovar, K. Lee, J. García-Antón, P. Schmuki. Formation of anodic TiO_2 nanotube or nanosponge morphology determined by the electrolyte hydrodynamic conditions, Electrochem. Commun. 26 (2013) 1.

[16] L. Aïnouche, L. Hamadou, A. Kadri, N. Benbrahim, D. Bradai. Interfacial Barrier Layer Properties of Three Generations of TiO_2 Nanotube Arrays, Electrochim. Acta 133 (2014) 597.

[17] D. Wang, X. Zhang, P. Sun, S. Lu, L. Wang, C. Wang, Y. Liu. Photoelectrochemical Water Splitting with Rutile TiO_2 Nanowires Array: Synergistic Effect of Hydrogen Treatment and Surface Modification with Anatase Nanoparticles, Electrochim. Acta 130 (2014) 290.

[18] R. Sánchez-Tovar, R. M. Fernández-Domene, D. M. García-García, J. García-Antón. Enhancement of photoelectrochemical activity for water splitting by controlling hydrodynamic conditions on titanium anodization, J. Power Sources 286 (2015) 224.

[19] S. J. Kim, J. Lee, J. Choi. Understanding of anodization of zinc in an electrolyte containing fluoride ions, Electrochim. Acta 53 (2008) 7941.

[20] N. K. Shrestha, K. Lee, R. Hahn, P. Schmuki. Anodic growth of hierarchically structured nanotubular ZnO architectures on zinc surfaces using a sulfide based electrolyte, Electrochem. Commun. 34 (2013) 9.

[21] W. Lee, D. Kim, K. Lee, P. Roy, P. Schmuki. Direct anodic growth of thick WO3 mesosponge layers and characterization of their photoelectrochemical response, Electrochim. Acta 56 (2010) 828.

[22] K. Kalantar-zadeh, A. Z. Sadek, H. Zheng, V. Bansal, S. K. Bhargava, W. Wlodarski, J. Zhu, L. Yu, Z. Hu. Nanostructured WO3 films using high temperature anodization, Sensor. Actuat. B-Chem. 142 (2009) 230.

[23] W. Li, J. Li, X. Wang, S. Luo, J. Xiao, Q. Chen. Visible light photoelectrochemical responsiveness of self-organized nanoporous WO_3 films, Electrochim. Acta 56 (2010) 620.

[24] C. K. Wang, C. K. Lin, C. L. Wu, S. C. Wang, J. L. Huang. Synthesis and characterization of electrochromic plate-like tungsten oxide films by acidic treatment of electrochemical anodized tungsten, Electrochim. Acta 112 (2013) 24.

[25] R. van de Krol, Y. Liang, J. Schoonman. Solar hydrogen production with nanostructured metal oxides, J. Mater. Chem. 18 (2008) 2311.

[26] K. Sivula, F. Le Formal, M. Grätzel. Solar Water Splitting: Progress Using Hematite (Fe_2O_3) Photoelectrodes, ChemSusChem 4 (2011) 432.

[27] J. Gan, X. Lu, T. Zhai, Y. Zhao, S. Xie, Y. Mao, Y. Zhang, Y. Yang, Y. Tong. Vertically aligned In_2O_3 nanorods on FTO substrates for photoelectrochemical applications, J. Mater. Chem. 21 (2011) 14685.

[28] R. Daghrir, P. Drogui, D. Robert. Photoelectrocatalytic technologies for environmental applications, J. Photoch. Photobio. A 238 (2012) 41.

[29] R. Sánchez-Tovar, I. Paramasivam, K. Lee, P. Schmuki. Influence of hydrodynamic conditions on growth and geometry of anodic TiO_2 nanotubes and their use towards optimized DSSCs, J. Mater. Chem. 22 (2012) 12792.

[30] N. Liu, K. Lee, P. Schmuki. Small diameter TiO_2 nanotubes vs. nanopores in dye sensitized solar cells, Electrochem. Commun. 15 (2012) 1.

[31] A. Valota, D. J. LeClere, P. Skeldon, M. Curioni, T. Hashimoto, S. Berger, J. Kunze, P. Schmuki, G. E. Thompson. Influence of water content on nanotubular anodic titania formed in fluoride/glycerol electrolytes, Electrochim. Acta 54 (2009) 4321.

[32] E. Binetti, Z. El Koura, N. Patel, A. Dashora, A. Miotello. Rapid hydrogenation of amorphous TiO_2 to produce efficient H-doped anatase for photocatalytic water splitting, Appl. Catal. A-General 500 (2015) 69.

[33] H. Lu, J. Zhao, L. Li, L. Gong, J. Zheng, L. Zhang, Z. Wang, J. Zhang, Z. Zhu. Selective oxidation of sacrificial ethanol over TiO2-based photocatalysts during water splitting, Energy Environ. Sci. 4 (2011) 3384.

[34] V. Tamilselvan, D. Yuvaraj, R. Rakesh Kumar, K. Narasimha Rao. Growth of rutile TiO_2 nanorods on TiO_2 seed layer deposited by electron beam evaporation, Appl. Surf. Sci. 258 (2012) 4283.

[35] P. Xiao, D. Liu, B. Batalla Garcia, S. Sepehri, Y. Zhang, G. Cao. Electrochemical and photoelectrical properties of titania nanotube arrays annealed in different gases, Sensor Actuat. B-Chem. 134 (2008) 367.

[36] W. H. Leng, Z. Zhang, J. Q. Zhang, C. N. Cao. Investigation of the Kinetics of a TiO_2 Photoelectrocatalytic Reaction Involving Charge Transfer and Recombination through Surface States by Electrochemical Impedance Spectroscopy, J. Phys. Chem. B 109 (2005) 15008.

[37] L. A. da Silva, V. A. Alves, M. A. P. da Silva, S. Trasatti, J. F. C. Boodts. Oxygen evolution in acid solution on IrO_2 + TiO_2 ceramic films. A study by impedance, voltammetry and SEM, Electrochim. Acta 42 (1997) 271.

[38] L.-K. Tsui, G. Zangari. Water content in the anodization electrolyte affects the electrochemical and electronic transport properties of TiO2 nanotubes: a study by electrochemical impedance spectroscopy, Electrochim. Acta 121 (2014) 203.

[39] D. P. Oyarzún, R. Córdova, O. E. Linarez Pérez, E. Muñoz, R. Henríquez, M. López Teijelo, H. Gómez. Morphological, electrochemical and photoelectrochemical characterization of nanotubular TiO_2 synthetized electrochemically from different electrolytes, J. Solid State Electrochem. 15 (2011) 2265.

[40] X. Liu, J. Lin, Y. H. Tsang, X. Chen, P. Hing, H. Huang. Improved anatase phase stability in small diameter TiO_2 nanotube arrays for high performance dye-sensitized solar cells, J. Alloys Compd. 607 (2014) 50.

[41] Y. Yang, X. Wang, L. Li. Crystallization and Phase Transition of Titanium Oxide Nanotube Arrays, J. Am. Ceram. Soc. 91 (2008) 632.

[42] G. J. Brug, A. L. G. van den Eeden, M. Sluyters-Rehbach, J. H. Sluyters. The analysis of electrode impedances complicated by the presence of a constant phase element, J. Electroanal. Chem. 176 (1984) 275.

[43] B. Hirschorn, M. E. Orazem, B. Tribollet, V. Vivier, I. Frateur, M. Musiani. Determination of effective capacitance and film thickness from constant-phase-element parameters, Electrochim. Acta 55 (2010) 6218.

[44] I. Paramasivam, H. Jha, N. Liu, P. Schmuki. A Review of Photocatalysis using Self-organized TiO_2 Nanotubes and Other Ordered Oxide Nanostructures, Small 8 (2012) 3073.

[45] D. Regonini, A. Jaroenworaluck, R. Stevens, C. R. Bowen. Effect of heat treatment on the properties and structure of TiO_2 nanotubes: phase composition and chemical composition, Surf. Interface Anal. 42 (2010) 139.

[46] M. Radecka, M. Rekas, A. Trenczek-Zajac, K. Zakrzewska. Importance of the band gap energy and flat band potential for application of modified TiO_2 photoanodes in water photolysis, J. Power Sources 181 (2008) 46.

[47] R. M. Fernández-Domene, E. Blasco-Tamarit, D. M. García-García, J. García-Antón. Passivity Breakdown of Titanium in LiBr solutions, J. Electrochem. Soc. 161 (2014) C25.

[48] D. Sazou, K. Saltidou, M. Pagitsas. Understanding the effect of bromides on the stability of titanium oxide films based on a point defect model, Electrochim. Acta 76 (2012) 48.

[49] H. Peng. First-principles study of native defects in rutile TiO_2, Phys. Lett. A 372 (2008) 1527.

[50] Z. Jiang, X. Dai, H. Middleton. Investigation on passivity of titanium under steady-state conditions in acidic solutions, Mater. Chem. Phys. 126 (2011) 859.

[51] D. S. Kong, W. H. Lu, Y. Y. Feng, Z. Y. Yu, J. X. Wu, W. J. Fan, H. Y. Liu. Studying on the Point-Defect-Conductive Property of the Semiconducting Anodic Oxide Films on Titanium, J. Electrochem. Soc. 156 (2009) C39.

[52] H. Irie, Y. Watanabe, K. Hashimoto. Nitrogen-Concentration Dependence on Photocatalytic Activity of $TiO_{2-x}N_x$ Powders, J. Phys. Chem. B 107 (2003) 5483.

[53] B. J. Morgan, G. W. Watson. Polaronic trapping of electrons and holes by native defects in anatase TiO_2, Phys. Rev. B 80 (2009) 233102.

Tables captions

Table 1. Equivalent circuit parameters for TiO_2 nanostructures (nanotubes and nanosponges) at different values of Re.

Table 2. Values of N_D and U_{FB} for the different anatase/rutile mixed TiO_2 nanostructures anodized under static (Re = 0) and hydrodynamic (Re > 0) conditions.

Table 3. Comparison between the photocurrents measured at 0.5 $V_{Ag/AgCl}$ for the systems anatase TiO_2 nanostructures and anatase/rutile mixed TiO_2 nanostrustures, at different Re.

Figures captions

Figure 1. Current density transients obtained during the potentiostatic anodization of Ti at 30 V at different Re.

Figure 2. FE-SEM images of the top-view of the TiO_2 nanotubes (Re = 0, image a) and nanosponges (Re from 100 to 500, images b to f) anodized at 30V, for 3 h, and cross sectional views of the nanotubes and nanosponges (at Re = 500).

Figure 3. Thickness of the nanotubes (Re = 0) and nanosponges (Re > 0) vs Re.

Figure 4. Raman confocal laser spectra of the amorphous nanotubes and annealed (650 ºC-1 h) TiO_2 nanotubes (Re = 0) and nanosponges (Re = 500) anodized at 30 V, for 3 h. The letter A indicates anatase and the letter R indicates rutile.

Figure 5. Experimental Nyquist (a), Bode-phase (b) and Bode-module (c) plots for the samples anodized from Re = 0 to Re = 500; (d) electrical equivalent circuit used to simulate experimental EIS data.

Figure 6. Mott-Schottky plots of the different anatase/rutile mixed TiO_2 nanostructures anodized under static (Re = 0) and hydrodynamic (Re > 0) conditions.

Figure 7. Current density vs. applied potential curves under dark and illumination conditions for the different anatase/rutile mixed TiO_2 nanostructures anodized under static (Re = 0) and hydrodynamic (Re > 0) conditions.

Figure 8. Photostability of the different anatase/rutile mixed TiO_2 nanostructures anodized under static (Re = 0) and hydrodynamic (Re > 0) conditions.

Figure 1

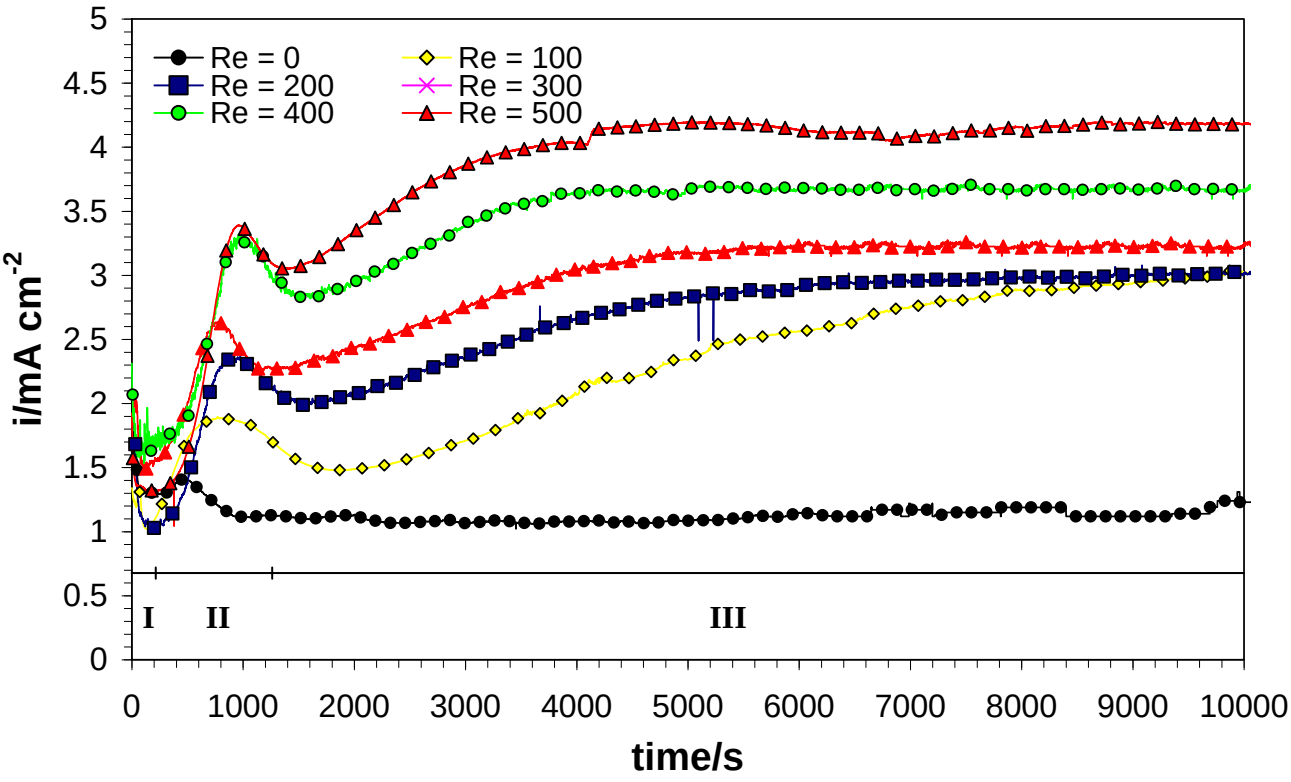
Re = 0
Re = 100
Re = 200
Re = 300
Re = 400
Re = 500
i/mA cm-2
time/s
I
II
III
0
0.5
1
1.5
2
2.5
3
3.5
4
4.5
5
0
1000
2000
3000
4000
5000
6000
7000
8000
9000
10000

Figure 2

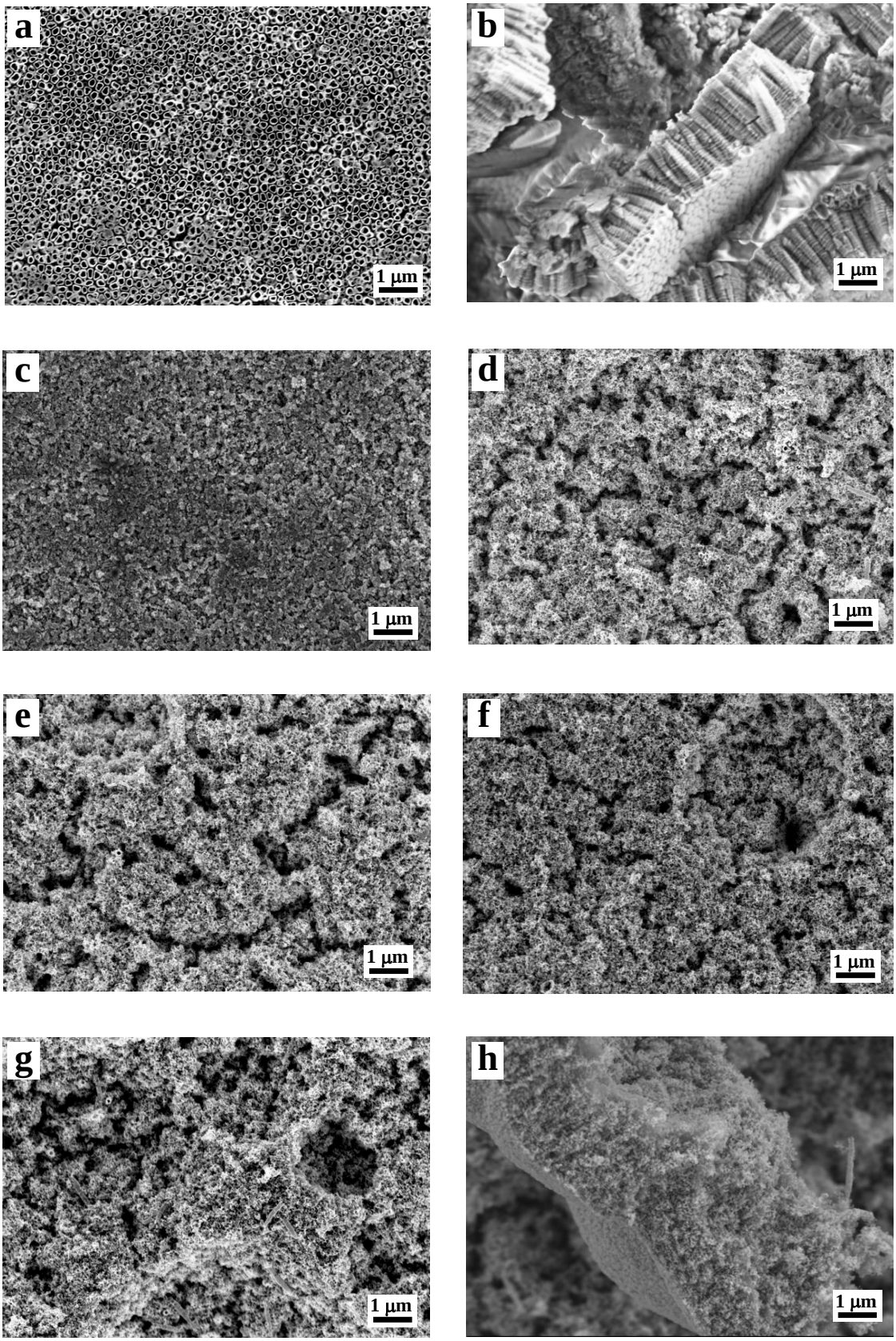

Figure 3

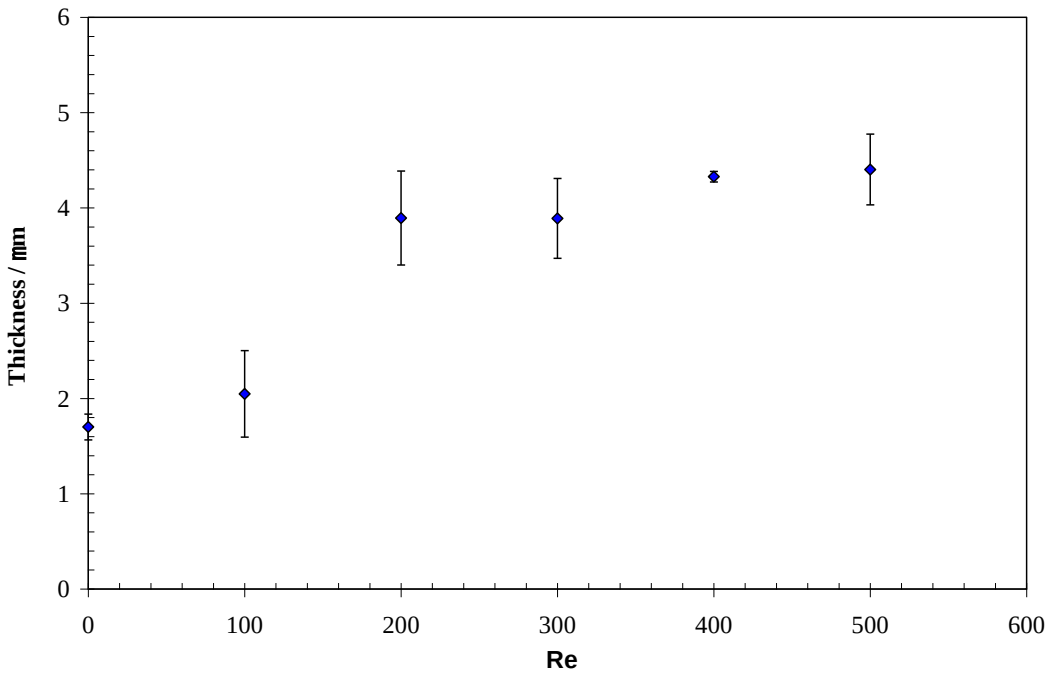

Figure 4

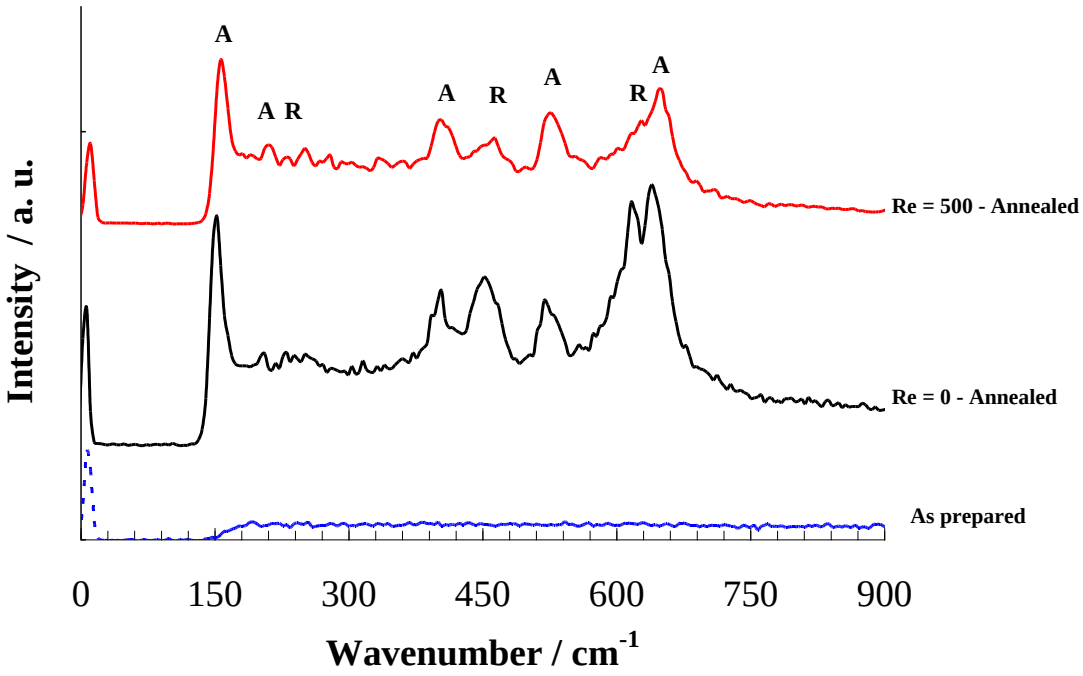
A
A R
A
R
A
R
A
Re = 500 - Annealed
Re = 0 - Annealed
As prepared
Intensity / a. u.
0
150
300
450
600
750
900
Wavenumber / cm-1

Figure 5

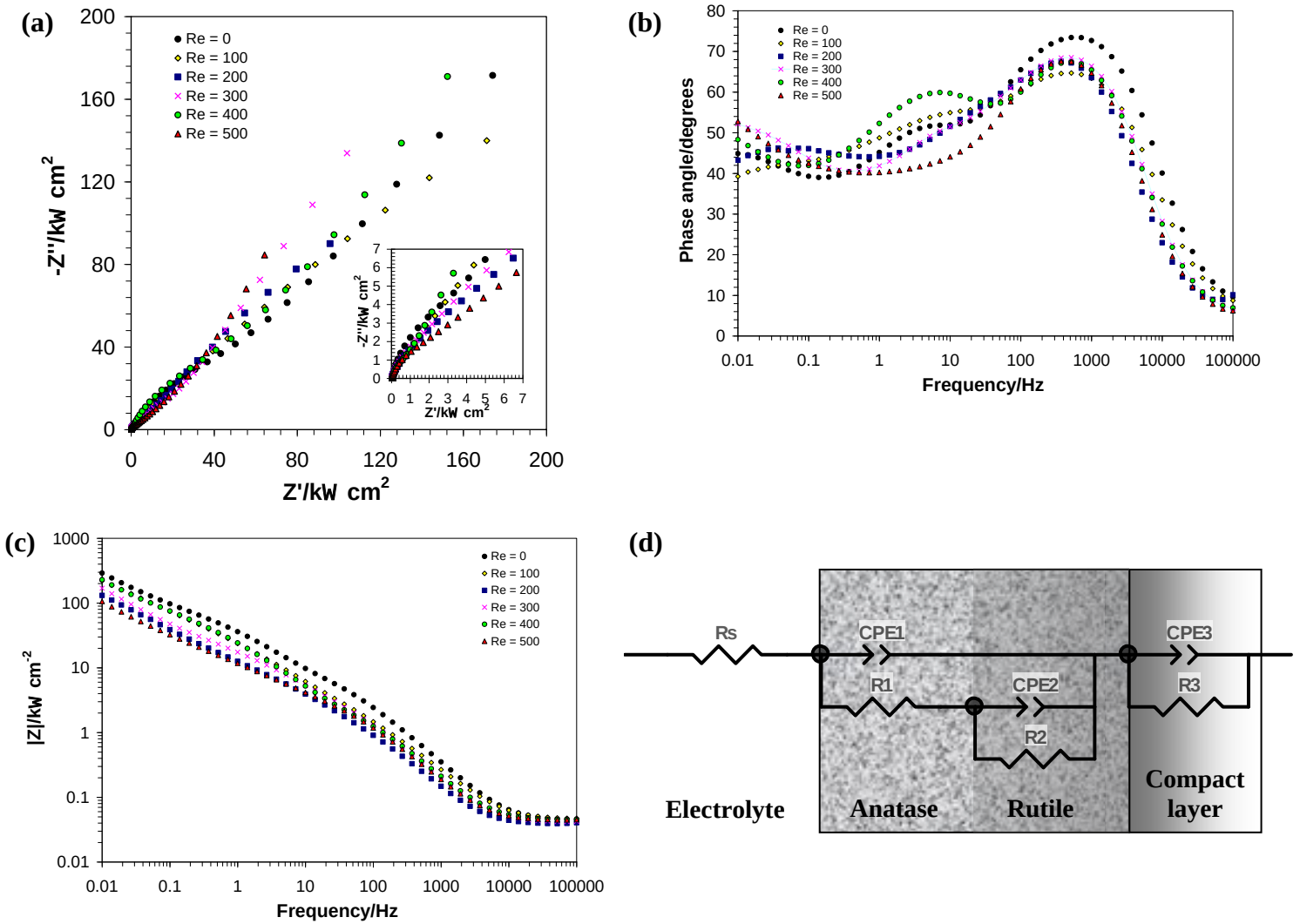
(a)
Re = 0
Re = 100
Re = 200
Re = 300
Re = 400
Re = 500
-Z''/kW cm2
Z'/kW cm2
(b)
Phase angle/degrees
Frequency/Hz
(c)
|Z|/kW cm-2
Frequency/Hz
(d)
Rs
CPE1
R1
CPE2
R2
CPE3
R3
Electrolyte
Anatase
Rutile
Compact layer

Figure 6

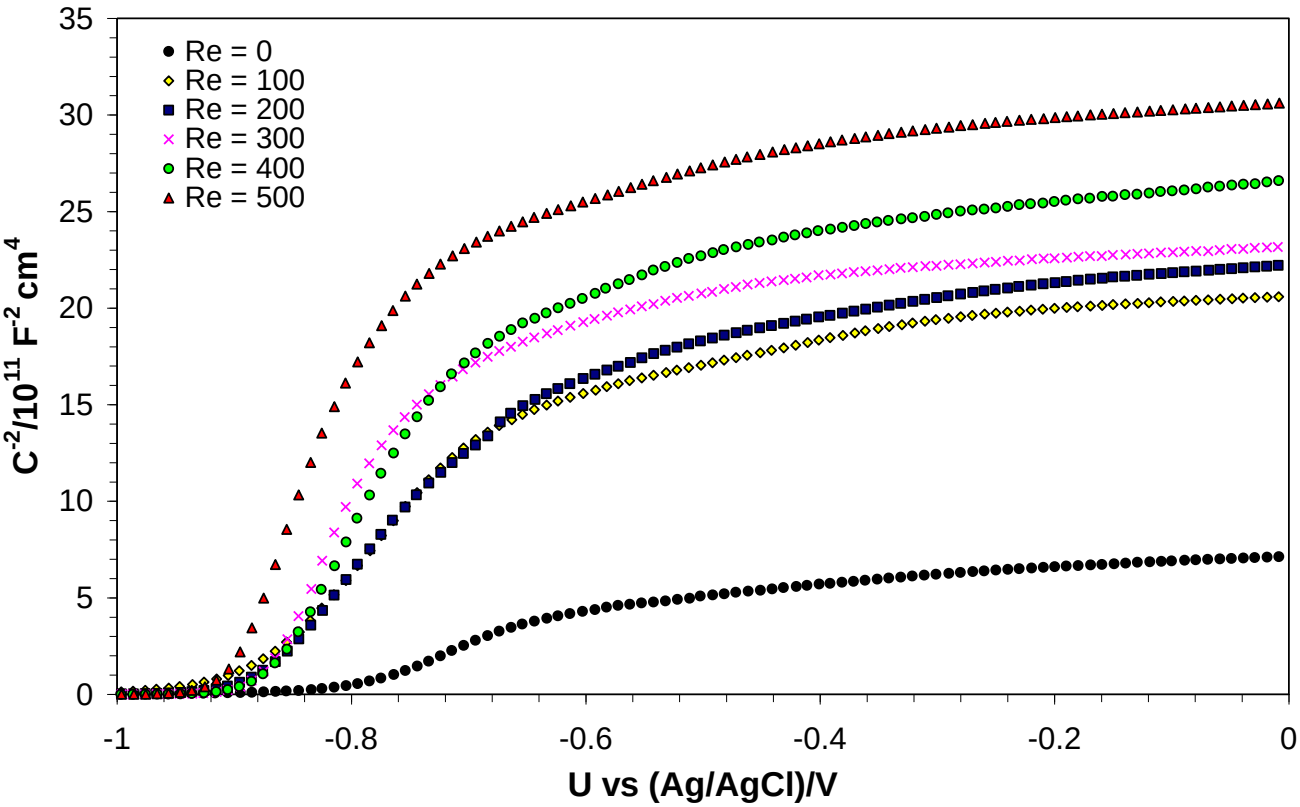
Re = 0
Re = 100
Re = 200
Re = 300
Re = 400
Re = 500
C-2/10^11 F-2 cm4
U vs (Ag/AgCl)/V
35
30
25
20
15
10
5
0
-1
-0.8
-0.6
-0.4
-0.2
0

Figure 7

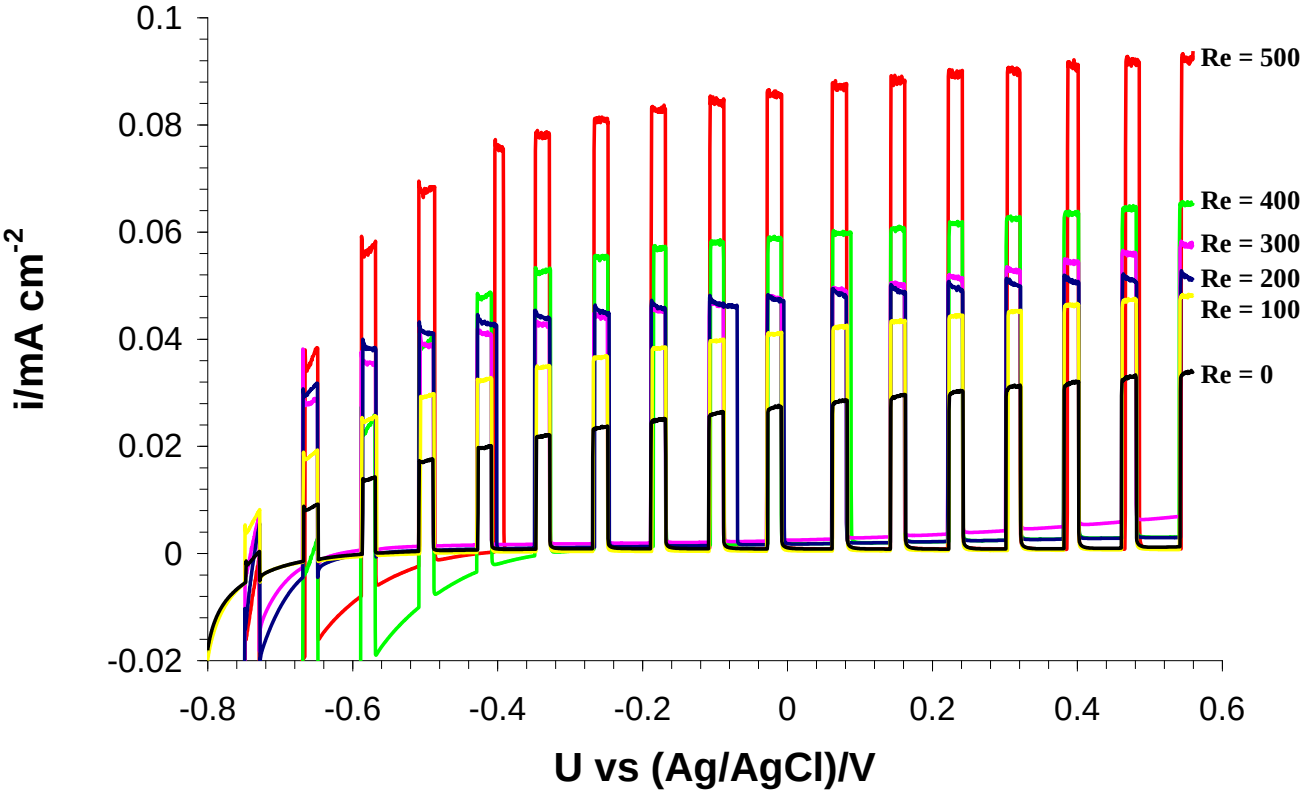
0.1
0.08
0.06
0.04
0.02
0
-0.02
i/mA cm-2
-0.8
-0.6
-0.4
-0.2
0
0.2
0.4
0.6
U vs (Ag/AgCl)/V
Re = 500
Re = 400
Re = 300
Re = 200
Re = 100
Re = 0

Figure 8

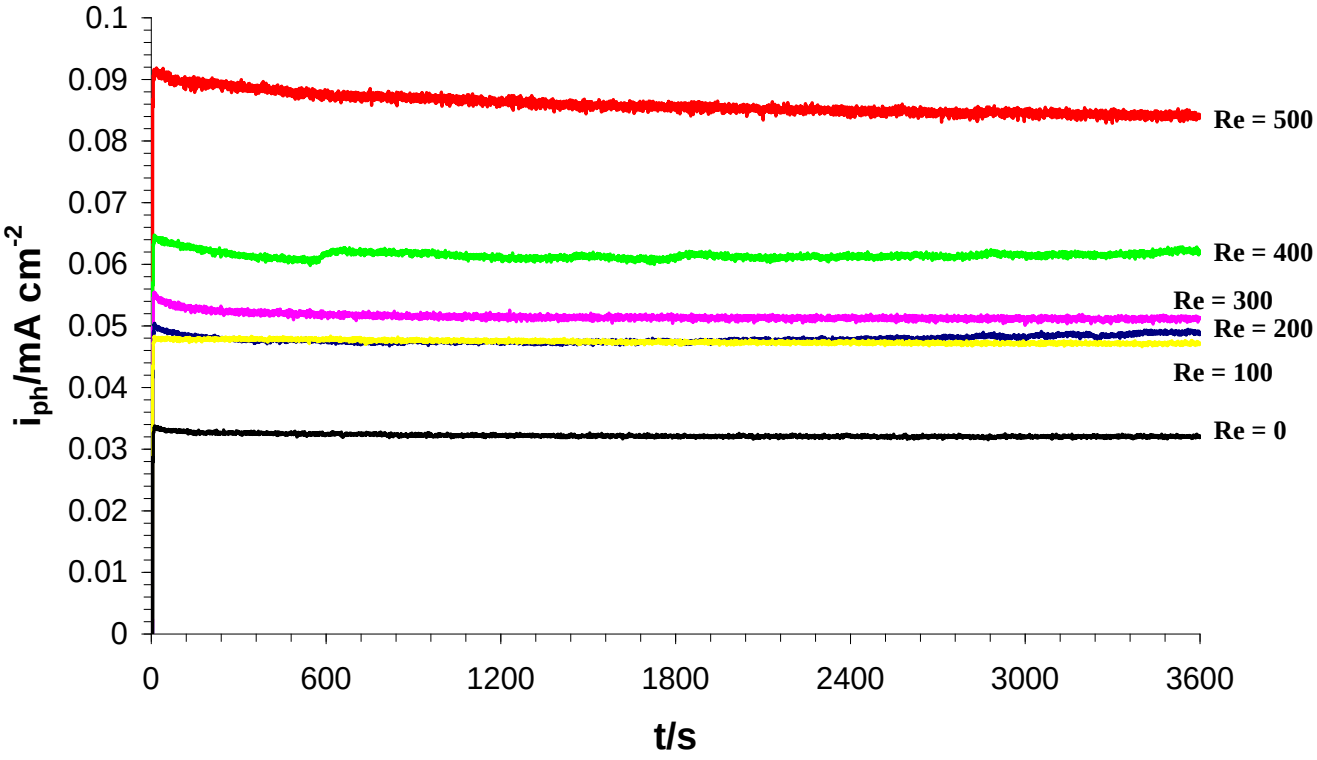
0.1
0.09
0.08
0.07
0.06
0.05
0.04
0.03
0.02
0.01
0
i_{ph}/mA cm^{-2}
0
600
1200
1800
2400
3000
3600
t/s
Re = 500
Re = 400
Re = 300
Re = 200
Re = 100
Re = 0

Table 1

Re	R_S/Ω cm^2	C_1/μF cm^{-2}	α_1	R_1/kΩ cm^2	C_2/μF cm^{-2}	α_2	R_2/kΩ cm^2	C_3/μF cm^{-2}	α_3	R_3/kΩ cm^2	χ^2 (x10^{-4})
0	43 ± 3	0.5 ± 0.9	0.96 ± 0.02	4.6 ± 2.1	6 ± 2	0.65 ± 0.07	64 ± 14	97 ± 43	0.73 ± 0.02	1140 ± 102	3
100	44 ± 5	0.7 ± 0.0	0.93 ± 0.03	1.2 ± 0.1	18 ± 1	0.57 ± 0.06	58 ± 10	115 ± 50	0.70 ± 0.02	609 ± 45	2
200	43 ± 8	0.6 ± 0.2	0.91 ± 0.06	1.2 ± 0.8	39 ± 10	0.46 ± 0.01	32 ± 9	286 ± 68	0.87 ± 0.01	421 ± 35	3
300	40 ± 1	1.2 ± 0.1	0.94 ± 0.03	1.1 ± 0.1	18± 4	0.49 ± 0.08	24 ± 7	324 ± 65	0.71 ± 0.09	813 ± 94	1
400	43 ± 3	1.1 ± 0.1	0.99 ± 0.03	1.1 ± 0.6	10 ± 2	0.71 ± 0.05	48 ± 15	165 ± 70	0.71 ± 0.01	1437 ± 210	3
500	43 ± 3	1.0 ± 0.1	0.97 ± 0.04	1.1 ± 0.4	50 ± 11	0.46 ± 0.09	26± 4	669 ± 91	0.69 ± 0.02	1950 ± 182	2